

**Adhesion-dependent negative friction coefficient on chemically-modified graphite at the
nanoscale**

Zhao Deng^{1,2}, Alex Smolyanitsky³, Qunyang Li⁴, Xi-Qiao Feng⁴ and Rachel J. Cannara^{1*}

¹Center for Nanoscale Science and Technology, National Institute of Standards and Technology,
Gaithersburg, MD 20899

²Maryland NanoCenter, University of Maryland, College Park, MD 20742

³Material Measurement Laboratory, National Institute of Standards and Technology, Boulder, CO
80305

⁴Center for Nano and Micro Mechanics, Applied Mechanics Laboratory, Department of
Engineering Mechanics, School of Aerospace, Tsinghua University, Beijing 100084 P.R. China

* rachel.cannara@nist.gov

From the early tribological studies of Leonardo da Vinci to Amontons' law, friction has been shown to increase with increasing normal load. This trend continues to hold at the nanoscale, where friction can vary nonlinearly with normal load^{1,2}. Here we present nanoscale friction force microscopy (FFM) experiments for a nanoscale probe tip sliding on a chemically-modified graphite surface in an atomic force microscope (AFM). Our results demonstrate that, when adhesion between the AFM tip and surface is enhanced relative to the exfoliation energy of graphite, friction can increase as the load decreases under tip retraction. This leads to the emergence of an effectively negative coefficient of friction in the low load regime. We show that the magnitude of this coefficient depends on the ratio of tip-sample adhesion to the exfoliation energy of graphite. Through both atomistic- and continuum-based simulations, we attribute this unusual phenomenon to a reversible partial exfoliation of the topmost atomic layers

which then mimic few- to single-layer graphene. Lifting of these layers with the AFM tip leads to greater deformability of the surface with decreasing applied load. This discovery suggests that the lamellar nature of graphite yields nanoscale tribological properties outside the predictive capacity of existing continuum mechanical models.

Carbon-based materials such as graphite, diamond, graphene, and carbon nanotubes have been the subject of ongoing interest for their unique electrical, thermal and mechanical properties³⁻⁶. Of particular interest are those attributes that enable graphite or graphene's use technologically as a lubricant and concurrently offer a unique platform to study the fundamental properties of friction and interlayer interactions. Recent studies of graphite and other lamellar materials have revealed an increase of friction with decreasing number of atomic layers⁷⁻⁹. The effect was ascribed to greater electron-phonon coupling for single-layer graphene^{7,8} and to the susceptibility of thinner layers to out-of-plane elastic deformation⁹. These nanoscale measurements are challenging, as both friction and adhesion are very small and the average friction force does not vary significantly with load^{7,10,11}. Consequently, the impact of adhesion on friction has not been as well investigated for graphite as for other materials.

Here we investigate the effect of adhesion on graphite's frictional properties by systematically varying tip-surface adhesion and measuring friction as a function of both applied normal load and adhesive force. Figures 1a and 1b show friction data as a function of load obtained by sliding a 30 nm-radius ultrananocrystalline diamond (UNCD) AFM tip on a graphite surface. Fig. 1a shows representative data for the tip both approaching and retracting from the sample. Fig. 1b compares retract data for three different adhesion conditions, including the high adhesion case shown in Fig. 1a. Adhesion was varied by exposing a freshly cleaved graphite sample to oxygen for different times in dry nitrogen with $\approx 1\%$ (by weight) O_2 . We chose

exposure conditions with low oxygen levels and long exposure times to reproducibly control the effect of oxygen exposure on surface properties. In Fig. 1a, the approach data indicate that friction is increasing with load as expected for an enlarging contact area due to elastic deformation of the interface in the normal direction^{1,2}. While frictional forces are always positive (opposing the direction of motion), surprisingly, we found that when adhesion is high enough friction continues to increase linearly with decreasing load upon retraction of the tip, leading to a negative effective nanoscale friction coefficient (or slope), α . No decrease in friction was observed to follow this increase prior to pull-off. Data from sequential approach-retract cycles at the same location, as well as for alternating between two different locations on the surface, were reproducible and yielded the same trend. Data from multiple cycles of approaching and retracting before pull-off repeatedly retraced the initial negatively-sloped data (Supplementary Information (SI) section IV). Positive loads were kept sufficiently low such that no surface damage was observed, and α did not change with maximum applied normal load in this low load regime. Scanning electron micrographs of the tips showed no evidence of flake attachment or tip degradation (SI section II).

As shown in Fig. 1b, we found that the pull-off force, L_C , increases in magnitude with exposure of graphite to oxygen, leading to a simultaneous increase in the magnitude of α . Increases in $|L_C|$ also shifted the friction-load curves upward, as expected for a corresponding increase in the overall tip-surface contact area with greater adhesion. The increase in $|L_C|$, and thus $|\alpha|$, versus time suggested that surface oxygen content could be a critical factor impacting adhesion. To test this hypothesis, we deliberately exposed samples to the higher levels of oxygen present in laboratory air (Methods and SI section I). This aging process produced a wider range of L_C and α values, as shown in Fig. 2a. To understand the surface chemistry, we

performed x-ray photoemission spectroscopy (XPS) on parallel graphite samples exposed to laboratory air for various time periods. In Fig. 2b, the data are grouped according to oxygen content, which increased from ≈ 0 atomic (at.) % to ≈ 3.5 at. % over 300 h (Fig. S7). Oxygen 1s region scans (Fig. 2b inset) showed an emergence of peaks at approximately 532 eV and 533 eV, indicating that increased hydrophilicity due to oxygen chemisorption was occurring¹²⁻¹³. We believe this increase in surface oxygen has a strong impact on the adhesive properties, as parallel friction measurements showed a concurrent increase in $|\alpha|$ and $|L_C|$ with increasing oxygen content (Fig. 2b).

To further investigate the origin of the negative friction coefficient, we compared atomic level friction data with the average friction force. Fig. 3a shows representative friction loops at different loads, exhibiting the typical sawtooth waveform (stick-slip behavior) characteristic of lattice resolution imaging on graphite (Fig. S4 shows UNCD tip data). While the average slip height of individual stick-slip events decreased with decreasing load, as expected from a corresponding reduction in atomic corrugation at lower loads¹⁴, the width of the friction loops increased with decreasing load. In addition to friction measurements, we performed lateral stiffness measurements as a function of normal load^{15,16}. These low-noise measurements provide additional information about the behavior of the contact during the approach and retract cycle. While for isotropic materials the lateral stiffness typically scales with contact radius, for lamellar materials we posit that these data may also reveal load-dependent variations in the mechanical properties of the contact based on the number of surface and subsurface layers with which the tip effectively interacts. Fig. 3b shows representative lateral stiffness measurements performed on graphite surfaces exposed to laboratory air for different times. As exposure time and adhesion increase, the lateral contact stiffness transitions from decreasing with decreasing load with no

evidence of approach-retract hysteresis (the low adhesion case) to *increasing* with decreasing load (the high adhesion case) under retraction only. The correspondence between lateral stiffness and average friction in the case of high adhesion rules out that the negative coefficient arises from very small changes in peak friction values combined with a more significant *decrease* in lateral stiffness, an effect demonstrated elsewhere¹⁷.

Based on these results, we propose that the negative coefficient arises from load-dependent local and reversible delamination of the surface and near-surface layers of the material. During retraction, when the tip-surface work of adhesion exceeds the exfoliation energy of graphite, the tip lifts the surface graphene layer(s) and locally separates them from the bulk. Behaving increasingly like a monolayer as the load becomes more negative, the lifted upper layers are more susceptible to out-of-plane deformation than when they are firmly attached to the bulk. When the tip slides laterally, the axisymmetry of the lifted region is broken and a ripple can form at the front of the contact due to friction, as previously proposed for monolayer graphene⁹. To counteract sliding resistance, the driving force needs to (i) overcome interfacial friction within the contact, and (ii) laterally displace the lifted region (together with any ripple).

Following this lifting hypothesis, we compared the tip-surface work of adhesion values with the exfoliation energy of graphite. Based on previous experimental and theoretical studies, the surface binding potential (exfoliation energy) is approximately (52 ± 5) meV per atom¹⁸⁻²⁰ (or (307 ± 30) mJ/m²). We estimated the tip-sample work of adhesion, W , using two established continuum mechanics methods, describing a range of regimes for single asperity contacts^{1,2,21}. We find that for the UNCD tips used in Figs. 2a and 2b, at $L_C = -40$ nN and -100 nN, respectively, W ranges from (0.212 ± 0.036) J/m² to (0.283 ± 0.048) J/m² in both cases. (Uncertainties correspond to one standard deviation.) The upper abscissae in the figures

represent the larger extreme for W , using $W = -L_c / (1.5\pi R)$ (see SI section V)². While strictly for isotropic materials, these estimates for the work of adhesion fall within the same order of magnitude as the exfoliation energy of graphite. Further, we note that, if existing single-asperity continuum mechanical models break down for this interface, then the true contact area is less than these models would predict²², and our W values underestimate the true work of adhesion. Hence, without an established contact theory for lamellar materials, we restrict our estimation of work of adhesion to isotropic continuum models.

To model adhesion-dependent friction between an AFM tip and graphite, we simulated the tip-graphite sliding contact with different magnitudes of the tip-surface interaction using both molecular dynamics (MD) and finite element method (FEM) (Fig. 4). Both MD and FEM demonstrate that the topmost graphene layer(s) can be lifted by the tip when the tip-surface interaction is enhanced (Figs. 4a and 4c, respectively). Both simulations suggest that this partial and reversible delamination would lead to greater susceptibility of the lifted layer(s) to out-of-plane deformation as the tip retracts. As a consequence, tip-surface adhesion must exceed surface-bulk adhesion for the negative coefficient to emerge, as shown in Figs. 4b and 4d. Comparing MD and FEM results, the onset of the negative coefficient appears to be sensitive to the number of layers in the model. While only one layer is considered in FEM, adding some compliance in the FEM substrate would have led to a larger indent into the material, allowing a broader extent of the topmost layer(s) to attach to the tip under positive loads for an enhanced tip-surface interaction. The FEM movies S2-S5 and the schematic representation of multiple layers in Fig. 5 show the tip gathering the top layer in this way. However, the system in Fig. 5 consists of subsurface layers that are also attracted to the tip. During retraction, these layers can

lift away from the bulk at the periphery of the contact, even at positive loads when the central region of the contact zone remains depressed.

The MD simulations suggest three mechanisms by which energy losses occur: (i) conventional van der Waals bonding-debonding in the contact zone, (ii) continuous stretching and relaxation of interlayer bonds, and (iii) lateral displacement of the deformed region beneath the tip (a viscoelastic process that would occur even for a deformation moving through a single graphene sheet in the absence of a tip)²³. The tip-deformed region is shown in Fig. 4a for the top three layers and fivefold enhancement of the tip-graphene interaction energy relative to graphene-graphene. For negative applied loads and high tip-surface adhesion, the size of this deformation increases with decreasing load, leading to greater energy losses associated with mechanisms (ii) and (iii). Meanwhile, the contact area decreases slightly, *reducing* the impact of mechanism (i). In Fig. 4c, FEM further indicates that a ripple can form ahead of the tip during sliding. If measured from the top of the ripple to the tip apex, the height of this ripple increases only slightly as the tip lifts the surface layer away from the bulk (Fig. 4c and Movs. S2-S5). However, the overall height and width of the deformed region increase, leading to a slightly larger overall deformation that must be displaced laterally by the tip. Accordingly, the compressive contact area and friction grow larger with lifting.

The increase in lateral stiffness with decreasing load provides further evidence that the negative coefficient of friction is a result of a partial exfoliation of the topmost graphene layer(s): If one treats graphene layers as springs that add in series under a lateral load or shear stress, an increase in lateral contact stiffness would result from a continuous decrease in the effective number of layers with which the tip is mechanically connected during retraction. Further, while the lifted layer(s) are more susceptible to *out-of-plane* deformation, resistance to in-plane (lateral)

deformation may grow as a result of the ripple and the related increase in compressive area at the edge of the contact with lifting (Movs. S2-S5). We note that both friction and lateral stiffness follow a linear dependence on load during retraction. Linear friction may be represented by an existing model for plowing friction (SI section VII). Experimentally, the low adhesion case produces little load dependence. In contrast, both simulations produce positive coefficients in the positive load regime. However, as with FEM, the negative coefficients in the experiment are typically greater in magnitude than the high-load positive coefficients. High positive-load pressures in MD due to the smaller, flatter tip relative to the experiment (and FEM) may explain why the positive coefficients in MD are similar in magnitude to their negative counterparts and fail to reproduce experiment in the high-load regime for the low adhesion case. Experimentally, in the low-adhesion case the area-load relationship can be balanced by changes in lateral stiffness¹⁷, a feature not captured by continuum-based FEM. When adhesion is high, the emergent negative coefficient can extend into the positive load regime (Fig. 1). We surmise that the onset of the negative coefficient at positive loads is a result of the tip gathering conformal layers upon approach and then lifting a number of graphite layers as soon as it retracts (Fig. 5), as indicated by the hysteresis in the lateral stiffness data (Fig. 3b). In Fig S6, friction-load data for mono-, bi- and trilayer supported graphene show that the onset of the negative coefficient is shifted to lower loads for few-layer graphene relative to graphite, indicating that compliance and the number of subsurface layers interacting with the tip help determine the onset load.

In conclusion, we have measured adhesion-dependent negative friction coefficients for graphite surfaces during retraction of an AFM tip. Until now, no variable-load experiments have varied adhesion and included the attractive regime to reveal this unexpected friction-load hysteresis. Our MD results suggest that dissipation associated with interlayer bond stretching

and lateral displacement of the deformed region beneath the contact zone increases when the top layer of graphite is partially (locally and reversibly) delaminated by the AFM tip. On the other hand, the FEM simulations suggest an increase in the driving force needed to push the lifted region forward as the tip retracts. Both simulation approaches show that lifting of the topmost graphene layer is crucial to the experimentally observed effect, as it leads to greater energy loss associated with the displacement of the deformed region. These results for graphite suggest that the relationship between α and L_C might be used to determine exfoliation energies of similar systems experimentally, once general models for the contact mechanics between an AFM tip and a layered material are established.

Methods

Friction and lateral stiffness, as well as adhesive forces, were obtained on highly oriented pyrolytic graphite samples cleaved with adhesive tape in laboratory air ($\approx 25\%$ relative humidity (RH) at $\approx 21\text{ }^\circ\text{C}$). The applied load was varied in contact mode AFM, using a triangle wave to approach and retract the tip from the surface. The average friction force was calculated at each applied load step from the lateral force loop. Adhesive forces were determined from the applied load at which the AFM tip separates from the surface during retraction. The FFM experiments were performed using both silicon nitride and UNCD probes at room temperature in dry nitrogen (RH $< 1\%$), yielding similar results. All experimental details appear in the SI (section I).

We simulated FFM using MD and FEM, as described in detail in the SI (section I). For MD, the FFM experiment was modeled using a single-walled carbon nanotube with a cap radius of 0.6 nm, scanning five graphene layers at with a sliding speed of 5 m/s. All tip-sample and interlayer van der Waals interactions were modeled by a Lennard-Jones pair potential.

Additional simulations were performed with the tip-sample interactions increased two and five times the interlayer interaction. The FEM simulations employed a rigid tip of radius 30 nm sliding quasi-statically against a single layer of graphene supported by a rigid substrate. The in-plane stiffness and bending stiffness of graphene were chosen based on established values and represented by a continuum shell model. Tip-graphene and graphene-substrate interactions followed from a Lennard-Jones-based model. The ratio of tip-graphene to graphene-substrate interaction energies was increased from 1:1 to 2:1 and 3:1. Friction was introduced to the system using a constant shear strength of 30 MPa wherever the local normal stress was compressive within the tip-graphene interface.

References

1. Derjaguin, B. V., Muller, V. M. & Toporov, Yu. P. Effect of contact deformations on the adhesion of particles. *J. Colloid Interf. Sci.* **53**, 314-326 (1975).
2. Johnson, K. L., Kendall, K. & Roberts, A. D. Surface energy and the contact of elastic solids. *Proc. R. Soc. Lond. A* **324**, 301-313 (1971).
3. Prelas, G. A., Popovici, G. & Bigelow, L. K., Eds. *Handbook of Industrial Diamonds and Diamond Films* (Marcel Dekker, Inc., New York, NY 1998).
4. Dresselhaus, M. S. & Dresselhaus, G. Intercalation compounds of graphite. *Adv. Phys.* **51**, 1-186 (2002).
5. Geim, A. K. Graphene: status and prospects. *Science* **324**, 1530-1534 (2009).
6. Allen, M. J., Tung, V. C. & Kaner, R. B. Honeycomb carbon: a review of graphene. *Chem. Rev.* **110**, 132-145 (2010).

7. Filleter, T., McChesney, J. L., Bostwick, A., Rotenberg, E., Emtsev, K. V., Seyller, Th., Horn, K. & R. Bennewitz. Friction and dissipation in epitaxial graphene films. *Phys. Rev. Lett.* **102**, 086102 (2009).
8. Filleter, T. & Bennewitz, R. Structural and frictional properties of graphene films on SiC(0001) studied by atomic force microscopy. *Phys. Rev. B* **81**, 155412 (2010).
9. Lee, C., Li, Q., Kalb, W., Liu, X.-Z., Berger, H., Carpick, R. W. & Hone, J. Frictional characteristics of atomically thin sheets. *Science* **328**, 76-80 (2010).
10. Dienwiebel, M., Verhoeven, G. S., Pradeep, N., Frenken, J. W. M., Heimberg, J. A. & Zandbergen, H. W. Superlubricity of graphite. *Phys. Rev. Lett.* **92**, 126101 (2004).
11. Lee, H., Lee, N., Seo, Y., Eom, J. & Lee, S. Comparison of frictional forces on graphene and graphite. *Nanotechnology* **20**, 325701 (2009).
12. Marchon, B., Carrazza, J., Heinemann, H. & Somorjai, G. A. TPD and XPS studies of O₂, CO₂, and H₂O adsorption on clean polycrystalline graphite. *Carbon* **26**, 507-514 (1988).
13. Wang, S., Zhang, Y. Abidi, N. & Cabrales, L. Wettability and surface free energy of graphene films. *Langmuir* **25**, 11078 (2009).
14. Socoliuc, A., Bennewitz, R., Gnecco, E. & Meyer, E. Transition from stick-slip to continuous sliding in atomic friction: entering a new regime of ultralow friction. *Phys. Rev. Lett.* **92**, 134301 (2004).
15. Lantz, M. A., O'Shea, S. J., Hoole, A. C. F. & Welland, M. E. Lateral stiffness of the tip and tip-sample contact in frictional force microscopy. *Appl. Phys. Lett.* **70**, 970-972 (1996).
16. Carpick, R. W., Ogletree, D. F. & Salmeron, M. Lateral stiffness: A new nanomechanical measurement for the determination of shear strengths with friction force microscopy. *Appl. Phys. Lett.* **70**, 1548-1550 (1997).

17. Dong, Y., Perez, D., Voter, A. F. & Martini, A. The roles of statics and dynamics in determining transitions between atomic friction regimes. *Tribol. Lett.* **42**, 99-107 (2011).
18. Zacharia, R., Ulbricht, H. & Hertel, T. Interlayer cohesive energy of graphite from thermal desorption of polyaromatic hydrocarbons. *Phys. Rev. B* **69**, 155406 (2004).
19. Hasegawa, M., Nishidate, K. & Iyetomi, H. Energetics of interlayer binding in graphite: the semiempirical approach revisited. *Phys. Rev. B* **76**, 115424 (2007).
20. Spanu, L., Sorella, S. & Galli, G. Nature and strength of interlayer binding in graphite. *Phys. Rev. Lett.* **103**, 196401 (2009).
21. Grierson, D. S., Flater, E. E. & Carpick, R. W. Accounting for the JKR–DMT transition in adhesion and friction measurements with atomic force microscopy. *J. Adhesion Sci. Technol.* **19**, 291-311 (2005).
22. Mo, Y., Turner, K. T. & Szlufarska, I. Friction laws at the nanoscale. *Nature* **457**, 1116-1119 (2009).
23. Smolyanitsky, A., Killgore, J. P. & Tewary, V. K. Effect of elastic deformation on frictional properties of few-layer graphene. *Phys. Rev. B* **85**, 035412 (2012).

Acknowledgements

The authors thank Fred Sharifi for providing invaluable insights regarding this work, and Kristen Steffens for XPS measurements. We further thank Robert Carpick, Clelia Righi, and Jason Killgore for stimulating discussions. Nicolas Faralli created the rendering software used to visualize the MD simulations. Z.D. acknowledges support under the Cooperative Research Agreement between the University of Maryland and the National Institute of Standards and Technology (NIST) Center for Nanoscale Science and Technology, Award 70NANB10H193,

through the University of Maryland. This research was performed while A.S. held a National Research Council Postdoctoral Research Associateship at NIST. Q.L. and X.-Q.F. acknowledge support from the Thousand Young Talents Program (20121770071-320501002) and the 973 Program (2010CB631005 & 2012CB934101), respectively.

Author contributions

Z.D. performed the experiments. Z.D. and R.J.C. analyzed the data. A.S. devised and performed the molecular dynamics simulations. Q.L. devised and performed the finite element (FE) simulations. X.-Q. F. provided guidance for the FE simulations of Q.L. R.J.C. supervised the project. Z.D., A.S., Q.L., and R.J.C. discussed results, composed the manuscript, and contributed to revisions.

Additional information

The authors declare no competing financial interests. Supplementary information accompanies this paper on www.nature.com/naturematerials. Reprints and permissions information is available online at www.nature.com/reprints. Correspondence and requests for materials should be addressed to R.J.C.

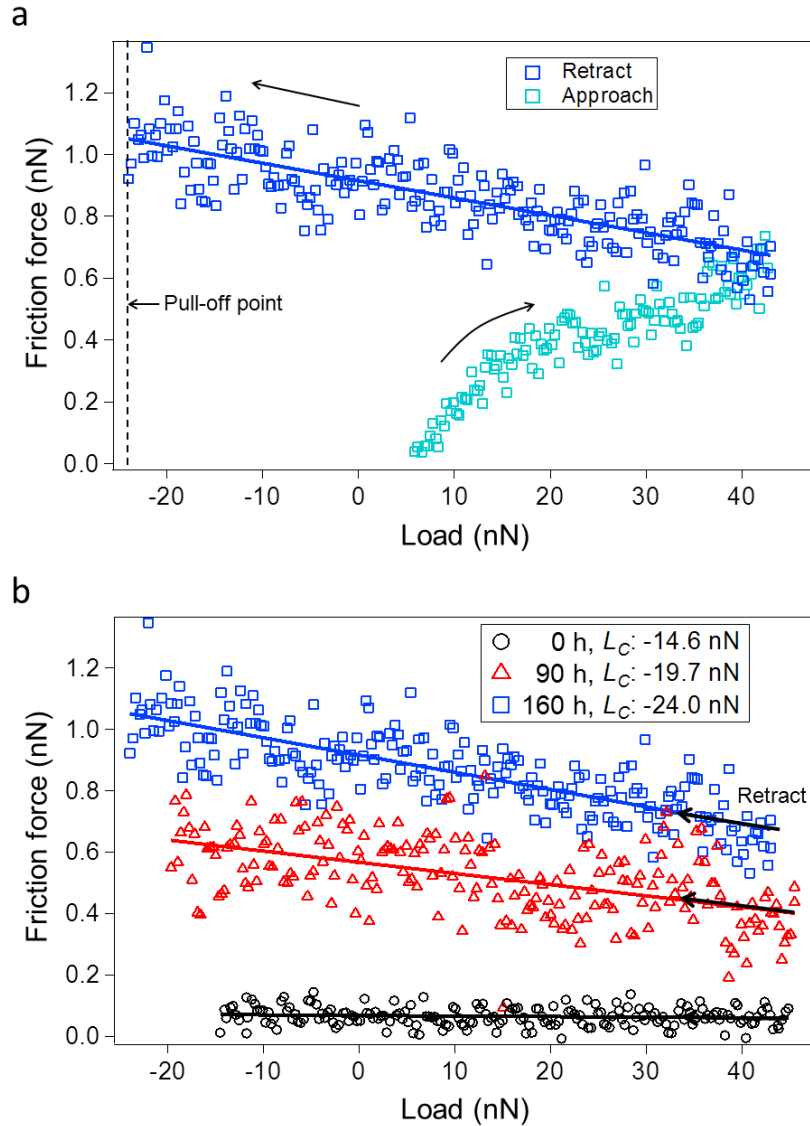


Figure 1 | Friction as a function of load and adhesive force. a, Friction-load curve, including both approach (light blue squares) and retract (dark blue squares) data. **b,** Friction data (unloading after loading) for the same tip and graphite surface under different aging conditions, including the retract curve shown in (a). Exposure times to low levels of oxygen are indicated in the legend. The scatter in these data arises from further inhomogeneities for different positions on the surface as sampled by the tip.

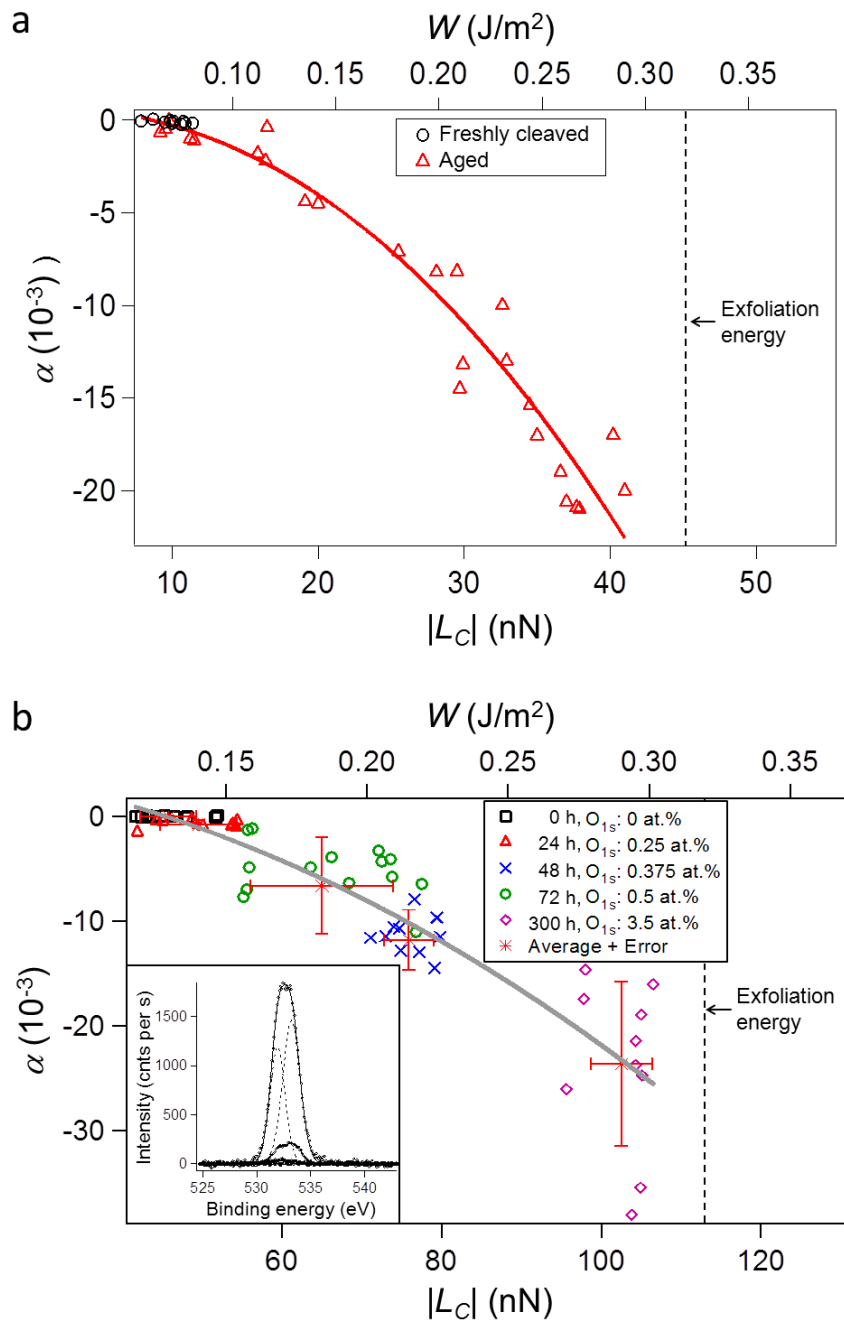


Figure 2 | Friction coefficient, α , as a function of the magnitude of the pull-off force, $|L_C|$, and work of adhesion, W . **a**, Data for the 30 nm UNCD tip on freshly cleaved (black circles) and aged (red triangles) graphite. **b**, α vs. $|L_C|$ for the 75 nm UNCD tip and different exposure times in laboratory air leading to variations in surface oxygen content. Inset: Parallel oxygen 1s (O_{1s}) region XPS data, where greater peak height corresponds to longer exposure time (Fig. S7).

Red asterices and error bars in (b) correspond to the average and standard deviation, respectively, for data from each time step. The solid lines are second order fits to the entire data set (as a visual guide). Uncertainties in the individual slope values are equal to or less than the size of the data points.

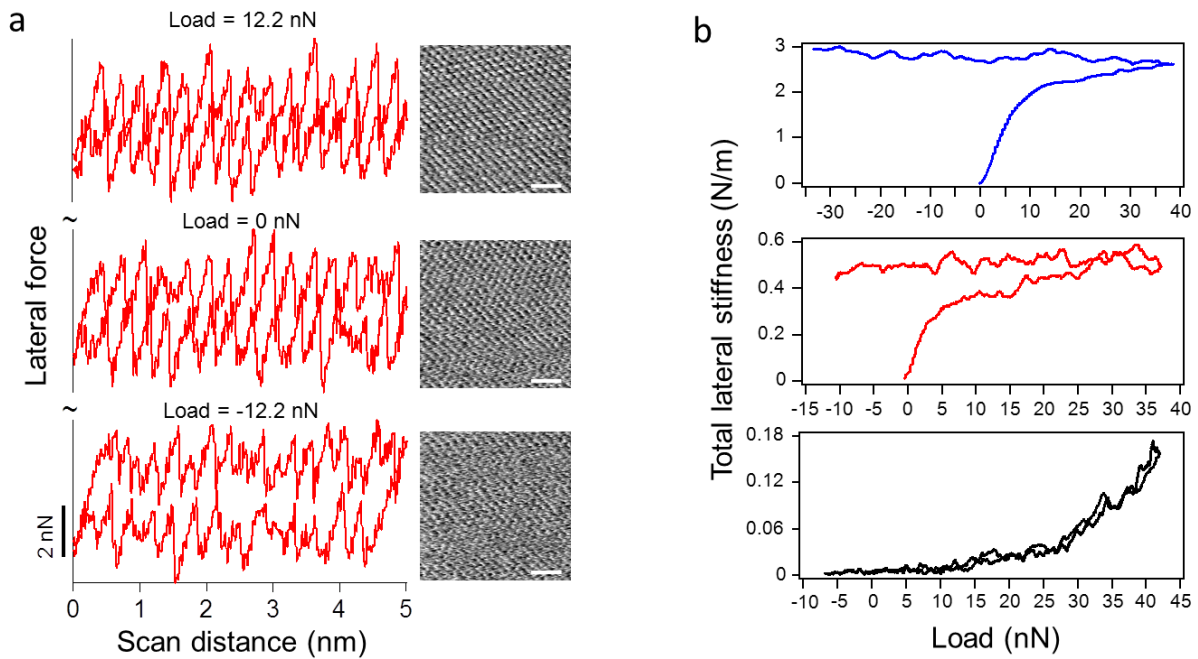


Figure 3 | Load-dependent stick-slip measurements. **a**, Atomic lattice stick-slip friction loops and corresponding friction force maps (scale bar = 1 nm) taken at three different applied loads (12.2 nN, 0 nN, and -12.2 nN) for the silicon nitride tip on graphite exposed to air for 190 h post cleavage. **b**, Lateral stiffness measurements as a function of applied load for the 30 nm UNCD tip on freshly cleaved (bottom, black), moderate adhesion (middle, red), and high adhesion (top, blue) cases, corresponding to approximately 0 h, 144 h, and 336 h, respectively. Note that the load axes cover different ranges. The total lateral stiffness consists of the cantilever lateral spring

constant in series with the tip structural stiffness and tip-sample contact stiffness; only the latter changes with load.

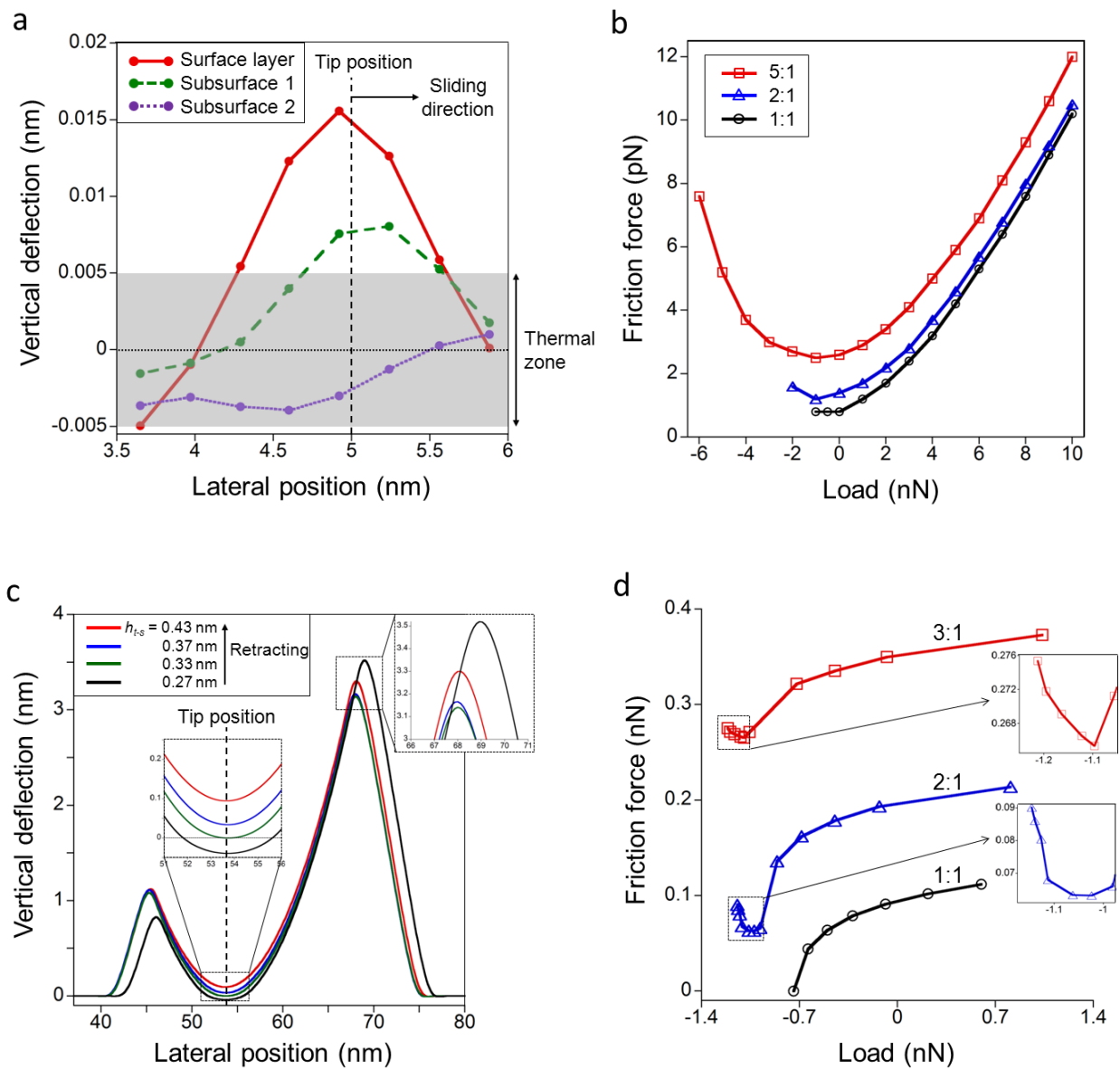


Figure 4 | MD and FEM simulations of friction between an AFM tip and graphite surface during tip retraction. a, Vertical deflection profiles (out-of plane deviation from average height) of the three topmost graphene layers in the MD simulation during sliding just prior to pull-off

(-6 nN applied load) for the 5:1 tip-graphene to graphene-graphene interaction ratio. (Fig. S9 includes profiles at 0 nN.) The subsurface layer profiles have been shifted upward to align the zero deflection positions of all three layers. The gray zone refers to the region over which thermally excited deflections occur naturally at room temperature. **b**, MD simulation results for friction as a function of applied load for three different interaction ratios (5:1, 2:1 and 1:1). The negative friction coefficient emerges when the tip-graphene interaction is greater than the graphene-graphene interaction. **c**, Vertical deflection profiles of the supported graphene layer simulated by FEM for different tip-substrate separations, h_{t-s} , where $h_{t-s} = 0$ would correspond to the tip apex touching the substrate, *i.e.*, pressing the graphene layer down by a full interlayer spacing. The tip slides to the right, as indicated by the asymmetry in the profiles. Adhesion between the tip and graphene layer is three times the graphene-substrate adhesion. **d**, FEM simulation results for friction as a function of applied load, as calculated from the average normal load in the contact zone, for three different interaction ratios (*i.e.*, tip-graphene adhesion is 1, 2 and 3 times the graphene-substrate adhesion). Insets are magnifications of the boxed negative-load regions for the twofold and threefold cases, for which effectively negative coefficients emerge. (Fig. S10 shows additional friction values as a function of both load and tip-substrate displacement, extending beyond the maximum tensile loads shown here. We note that the slope in the 2:1 case decreases beyond the pull-off point, as described therein.)

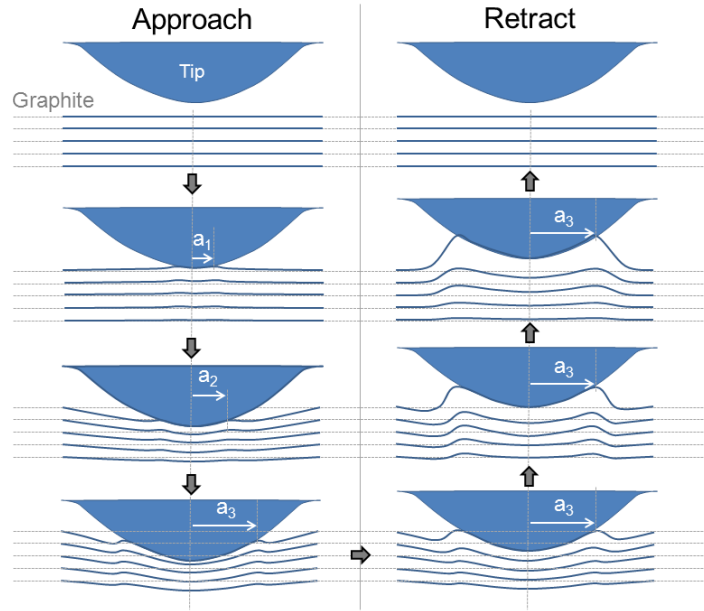


Figure 5 | Schematic representation of approach-retract hysteresis in the deformation of several surface and subsurface layers. This schematic illustrates the hysteresis in contact deformation that may be occurring based on the lateral stiffness and friction data, where approach-retract hysteresis in lateral stiffness corresponded to increases in friction with decreasing load. As the tip presses into the sample, the contact radius increases from a_1 to a_3 . For tip-graphene interaction energies larger than the interlayer interaction, the topmost layer(s) can conform to the tip and remain attached to it upon retraction. The tip gathers conformal layer(s) around its perimeter; once the tip begins to retract, the outermost rim of the top layer(s) can begin to lift away from its rest position. In the context of the FEM simulations, the compressive contribution of this outer rim to friction would compete with the contact area in the central compressive region, and thus would depend on the number of layers involved in the process.

Supplementary Information:

“Adhesion-dependent negative friction coefficient on chemically-modified graphite at the nanoscale”

Zhao Deng^{1,2}, Alex Smolyanitsky³, Qunyang Li⁴, Xi-Qiao Feng⁴ and Rachel J. Cannara^{1*}

¹Center for Nanoscale Science and Technology, National Institute of Standards and Technology,
Gaithersburg, MD 20899

²Maryland NanoCenter, University of Maryland, College Park, MD 20742

³Material Measurement Laboratory, National Institute of Standards and Technology, Boulder, CO 80305

⁴Center for Nano and Micro Mechanics, Applied Mechanics Laboratory, Department of Engineering
Mechanics, School of Aerospace, Tsinghua University, Beijing 100084 P.R. China

* rachel.cannara@nist.gov

I. METHODS

A. Friction force microscopy (FFM):

Friction and lateral stiffness as a function of load, as well as adhesive forces, were obtained on highly oriented pyrolytic graphite samples cleaved with adhesive tape in laboratory air ($\approx 25\%$ relative humidity (RH) at $\approx 21\text{ }^\circ\text{C}$). The applied load was varied by controlling the load in contact mode atomic force microscopy (AFM), using a triangle wave to approach and then retract the tip from the surface in a single image. The friction force was calculated at each applied load step, in the usual fashion, from the lateral force hysteresis loop. The average friction force was then calculated as half the difference between the trace and retrace lateral signals, to within a multiplicative lateral force calibration factor obtained using a diamagnetic lateral force calibrator^{S1}. Flexural spring constants were determined using the thermal noise method^{S2}. Load forces were calibrated in the usual way, by multiplying the flexural spring

constant by the deflection sensitivity (slope of the vertical force-displacement curve) on a stiff (SiO_2) surface. Adhesive forces were determined from the applied load at which the AFM tip separates from the surface during retraction.

The friction experiments were performed using both silicon nitride and ultrananocrystalline diamond (UNCD) probes at room temperature in dry nitrogen ($\text{RH} < 1\%$), yielding similar results. The silicon nitride probe of radius $R = (15 \pm 3)$ nm had a flexural stiffness $k_N = (0.72 \pm 0.03)$ N/m; the two UNCD probe radii were $R = (30 \pm 5)$ nm and (75 ± 7) nm with $k_N = (0.15 \pm 0.01)$ N/m and (0.120 ± 0.002) N/m, respectively. Radii were determined post-experiment by scanning electron microscopy. Uncertainties in R are based on one standard deviation. Uncertainties in k_N were obtained from the usual Taylor series expansion for experimental uncertainty analysis. Scan sizes were 10 nm, and scan speeds were 40 nm/s. The measurement error in the friction-load plots is comparable to the size of the data points, and the scatter in the data is due to small inhomogeneities of the sample, as each data point is measured on a slightly different scan line. Scatter in the data is least for freshly cleaved graphite, but surface inhomogeneities emerge over longer exposure times, leading to greater scatter.

The lateral stiffness measurements were performed as a function of load using a lock-in amplification technique described elsewhere^{S3,S4}. In this technique, the tip remains in static contact with the sample surface (*i.e.*, it does not slide) as the the sample is oscillated by a small amount in the lateral direction (parallel to the short axis of the cantilever). In the experiments here, we used a scanner oscillation rate of 1 kHz and a peak-to-peak amplitude of 0.56 nm, maintaining static contact. The AFM tip used to capture the data in Fig. 2b was the 30 nm UNCD probe described above.

B. Molecular Dynamics (MD) Simulations:

We simulated FFM using the MD setup as described in detail elsewhere^{S5}. As shown in Fig. S1 below, the simulated graphite sample consisted of five $5.5 \text{ nm} \times 6.2 \text{ nm}$ layers of graphene stacked in an ABAB order. The atoms at the edge of all layers in the x-direction and all atoms in the lowest layer were harmonically restrained in all three dimensions. A periodic boundary was imposed in the y-direction. A single-wall carbon nanotube (CNT) was used as the FFM tip scanning in the y-direction. The chirality, effective diameter, and height of the nanotube were (5,5), 1.2 nm, and 2.3 nm, respectively. During the simulated FFM scan, the upper half of the atoms along the height of the CNT were harmonically restrained and rigidly translated at a prescribed velocity of 5 m/s. The remaining atoms of the CNT interacted freely with the sample. A prescribed tip-sample contact force was maintained with feedback throughout each simulation. The contact force was varied from +10 nN in the repulsive (pushing) mode to the negative force in the adhesive (pulling) mode necessary to achieve loss of tip-sample contact (pull-off).

The carbon atoms within each layer of the sample and within the tip interacted via the bond-order potential^{S6}. All tip-sample and interlayer van der Waals interactions were modeled by a Lennard-Jones pair potential with $\epsilon = 7.5 \text{ meV}$ and $\sigma = 0.31 \text{ nm}$ and an interaction cut-off distance of 0.7 nm, yielding an interlayer cohesion of 42.8 meV/atom, in reasonable agreement with experiment and *ab initio* data^{S7-S9}. Additional simulations were performed with the tip-sample interactions increased two and five times the interlayer interaction. All simulations were performed at $T = 300 \text{ K}$, maintained by the Langevin thermostat, as described in ref. S5. All scans were performed during a simulated period of 1.0 ns, corresponding to a total scan distance

of 5.0 nm. The friction force averages were calculated from the last 750 ps of each simulation, allowing 250 ps for relaxation.

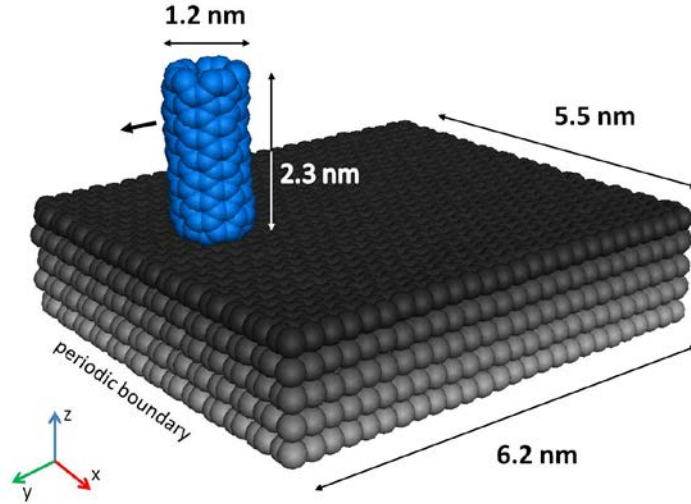


Figure S1 | The MD simulation setup using a CNT tip sliding along the y-direction at 5 m/s against the graphite surface, which consists of five layers of graphene stacked in ABAB order.

C. Finite Element Method (FEM) Simulations:

We used quasistatic FEM to simulate the process of an AFM tip scanning in contact with a graphite sample. For simplicity, we considered a two-dimensional case, where a cylinder rounded at its end (approximating the tip) slides against an elastic sheet, approximating the graphene layer(s), adhered to a substrate representing the graphite (Fig. S2). Both the tip and the substrate were assumed to be rigid. Tip-graphene and graphene-substrate interactions were prescribed by the cohesive zone model^{S10}, which is derived from a Lennard-Jones potential. More specifically, the interaction stress, $\bar{\sigma}$, between the elastic sheet (graphene) and the substrate as a function of inter-surface separation, δ , follows the form

$$\bar{\sigma} = 3.07\bar{\sigma}_0 \left(\frac{1}{(\delta/\delta_0)^4} - \frac{1}{(\delta/\delta_0)^{10}} \right), \text{ where } \delta_0 \text{ is the equilibrium separation. During the}$$

simulation, the tip was first brought into contact with the elastic sheet and compressed against the substrate. Then the tip was retracted partially to achieve the desired normal load before performing a lateral sliding at that constant height. As this is a displacement-controlled system, tip-substrate separations beyond the experimental pull-off can be probed theoretically. In the main text, the friction-load plots do not extend all the way to full separation, as the goal was to emphasize the existence of the negative coefficient and its onset prior to the experimental pull-off. (See section VIII.B below for more details.)

For the FEM simulations, the elastic sheet (graphene) and substrate were both 2 μm long and fixed at their edges, while the tip had a radius of 30 nm. The elastic sheet had an effective Young's modulus of 5.5 TPa and an effective thickness of 0.066 nm to represent the bending stiffness (0.85 eV) and in-plane stretching stiffness (within $340 \pm 50 \text{ N/m}^{\text{S11}}$) of monolayer graphene by a continuum shell model^{S12,S13}. The tip-graphene adhesion parameter, $\bar{\sigma}_0^{\text{t-g}}$, was assumed to be equal to or greater than the graphene-substrate adhesion parameter, $\bar{\sigma}_0^{\text{g-s}}$. We used $\bar{\sigma}_0^{\text{g-s}} = 150 \text{ MPa}$ and $\bar{\sigma}_0^{\text{t-g}}$ was varied from 150 MPa to 450 MPa to simulate the change in tip-sample adhesion. In the simulations, δ_0 was 0.33 nm for both interfaces. Note that the continuum approach demands the use of a much lower effective thickness than the interlayer spacing in order to comply with accepted values for the bending and in-plane stretching stiffness. Friction was introduced to the system using a constant shear strength of 30 MPa wherever the local normal stress was compressive within the tip-graphene interface. This value is within the range of values determined here experimentally for the shear strength of a silicon nitride tip sliding on supported monolayer graphene, as extracted from continuum fits to friction-load data.

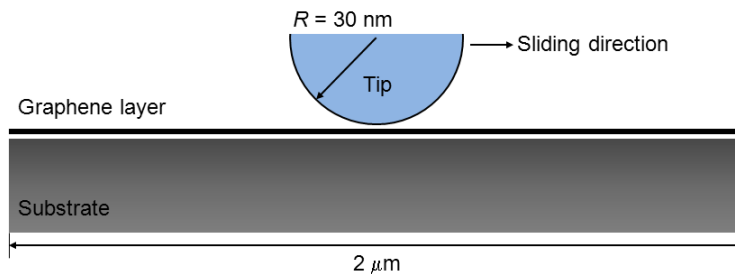


Figure S2 | FEM simulation setup, showing the 30 nm radius, rigid spherical tip and 2 μm rigid substrate with single graphene surface layer.

II. SEM IMAGES OF AFM PROBES

Figure S3 shows three post-experiment high magnification scanning electron microscopy (SEM) images of the atomic force microscopy (AFM) tips used in the experiment. Figs. S3a and S3b correspond to the ultrananocrystalline diamond (UNCD) probes (Advanced Diamond Technologies, Inc., Romeoville, IL)^{S14} used throughout the manuscript. Figure S3c shows the silicon nitride probe (Olympus, Tokyo, Japan)^{S14} used for acquiring the data in Fig. S6 below. In previous work, some cases have been shown to result in flakes adhered to the tip^{S15,S16}. Using SEM, we resolved no evidence of flake attachment. Moreover, we found that different sized tips extrapolated to the same friction coefficient at a given estimated work of adhesion (*e.g.*, at the graphite exfoliation energy) (Fig. 2). Accordingly, if the ripple effect were occurring in flakes attached to the tips, the flakes would then have to be of the same size. Instead, we found that adhesive forces were commensurate with tip radius, consistent with the interface occurring between the tip and sample surfaces and not a (flat) flake and sample surface.

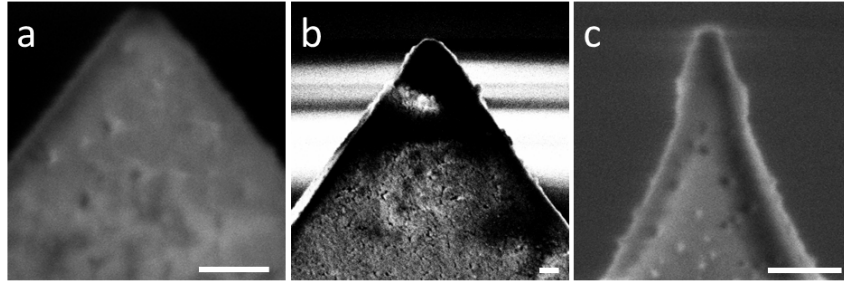


Figure S3 | SEM images of AFM tips used for acquiring friction-load curves. a, The UNCD AFM tip of radius, $R = (30 \pm 5)$ nm. **b,** The UNCD AFM tip with $R = (75 \pm 7)$ nm. **c,** The silicon nitride AFM tip of radius $R = (15 \pm 3)$ nm. All three images were taken at the end of their respective experiments. Scale bars: 100 nm.

III. STICK-SLIP FRICTION MEASUREMENTS

Figure S4 shows stick-slip friction loops on aged graphite at different applied loads during tip retraction, using the UNCD probe shown in Fig. S3b. Also considering the stick-slip data using the silicon nitride probe (main text, Fig. 3a), regardless of tip material the width of the friction loops decreases with increasing load, and the average slip height increases with applied normal load. We note that the friction loops of Fig. S4a exhibit some double-slip events due to the softer cantilever and larger tip size relative to the silicon nitride probe. Figure S4b shows a plot of the lateral forces in Fig. S4a as a function of applied load, where we compare slip height with the overall friction force (one-half times trace minus retrace). Slip heights decrease with decreasing load due to changes in atomic corrugation, as shown elsewhere^{S17-S19}.

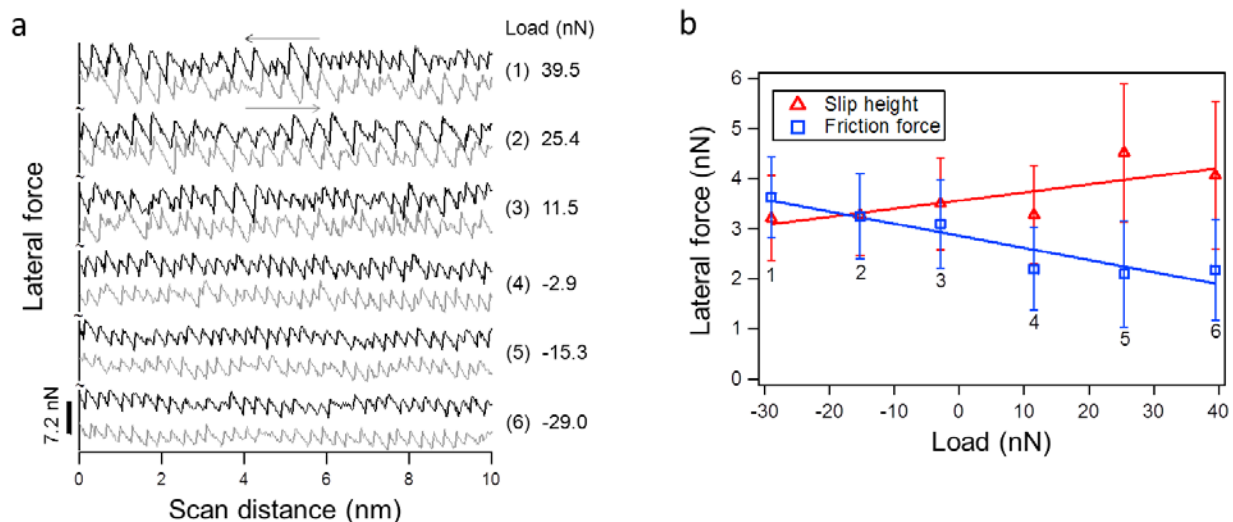


Figure S4 | Load dependence of atomic friction. **a**, Stick-slip friction loops at different applied loads (right), using the 30 nm-radius UNCD probe on aged graphite; trace (black) and retrace (gray) directions are indicated by the arrows. **b**, Slip height (open red triangles) and average friction force (open blue squares) as a function of load, corresponding to the friction loops in (a).

IV. CYCLING OF FRICTION-LOAD MEASUREMENTS

Cycled load-variation experiments were performed on an aged graphite surface using the 30 nm-radius UNCD probe. To test whether the observed friction-load relationship is reversible, we cycled the load multiple times. Figure S5a shows both friction and applied load for two such cycles as a function of time (represented by scan line); the direct plot of friction versus load for these data (Fig. S5b) shows that the negative coefficient is reproducible. Friction increases with load during the first tip approach and subsequently decreases with load and retraces itself thereafter with repeated cycling of the load. The repeatability of the initial retraction data supports reversible partial exfoliation and eliminates tip or sample damage as the main effect.

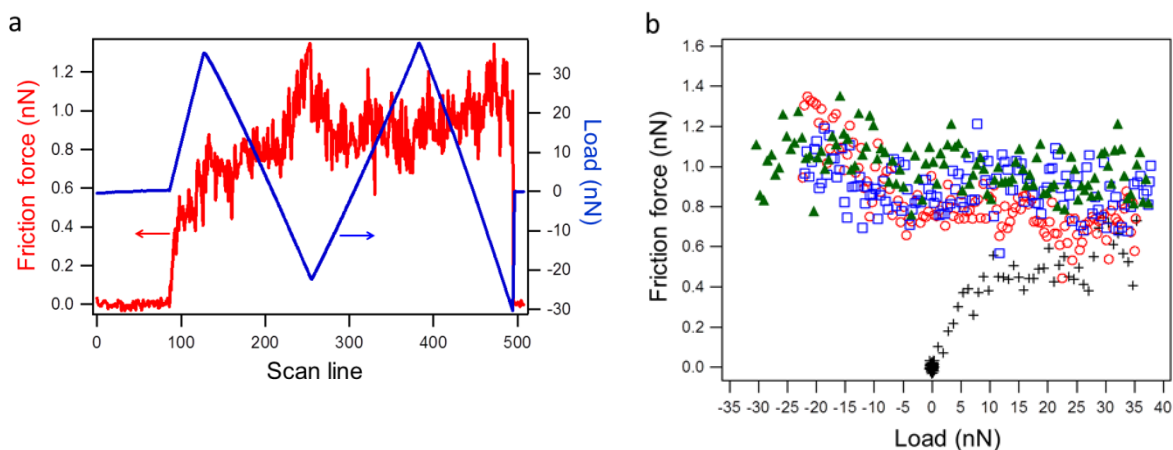


Figure S5 | Reversible friction-load curves on graphite. **a**, Friction force and applied load plotted as a function of scan line, using the 30 nm-radius UNCD probe, where the load was cycled through approach and retract twice before pulling off (1st approach = black crosses, 1st retract = open red circles, 2nd approach = open blue squares, and 3rd retract = solid green triangles). Each data point (image scan line) corresponds to an elapsed time of 0.5 s. **b**, The same data in (a) replotted as a function of load instead of scan line. The cluster of data at (0, 0) are the out-of-contact data recorded during the initial approach.

V. NEGATIVE FRICTION COEFFICIENT ON SUPPORTED MULTILAYER GRAPHENE AND THE APPLICATION OF CONTINUUM MODELS

Figure S6 shows three representative friction-load curves taken with a silicon nitride probe in ambient air on supported trilayer, bilayer and monolayer regions of graphene. The graphene flakes were prepared by mechanical exfoliation of natural graphite onto the surface of a 300 nm-thick silicon dioxide layer on silicon substrate and exposed to laboratory air for > 300 h. The number of graphene layers were measured based on AFM topography and Raman spectra. Figure S6a shows a slightly negative slope of the friction-load curve on the graphene trilayer, while friction increased with load for bilayer and monolayer graphene. As a result of stronger adhesion of the monolayer to the SiO₂ substrate compared with the graphene-graphene

exfoliation energy, no lifting occurs until there are a sufficient number of subsurface graphene layers. In the main text, we calculate the exfoliation energy to be $\approx 0.32 \text{ J/m}^2$; whereas, monolayer-SiO₂ adhesion of 0.45 J/m^2 has been demonstrated elsewhere, based on experiments on pressurized graphene membranes^{S20}. We note that the bilayer exhibits a possible onset in the negative load regime starting from -5 nN (Fig. S6b).

In the main text, we estimate the tip-sample work of adhesion based on continuum Johnson-Kendall-Roberts (JKR) theory^{S21}. This is based on the fact that we observe a trend toward JKR-like behavior for single layer graphene supported by SiO₂. Further, when compared with the exfoliation energy of 0.319 J/m^2 , the JKR limit more closely predicts the force required to exfoliate a surface graphite layer. A reduction in interlayer binding by $W = 0.283 \text{ J/m}^2$ corresponds to a separation of the graphite layer from its equilibrium spacing by $\approx 0.32 \text{ nm}$, or nearly one layer spacing^{S8}. This reversible partial exfoliation is exemplified in Fig. 2, where $|\alpha|$ increases faster with $|L_C|$ as the tip-surface work of adhesion approaches the exfoliation energy. Given that our MD and FEM results predict the tip-sample work of adhesion must be *enhanced* relative to the exfoliation energy for lifting to occur, it should be surprising that the tribomechanical behavior of the graphite surface mimics that of single layer of graphene under tip retraction when the work of adhesion is simply comparable to the exfoliation energy. However, we emphasize that our experimental adhesion values represent a lower limit.

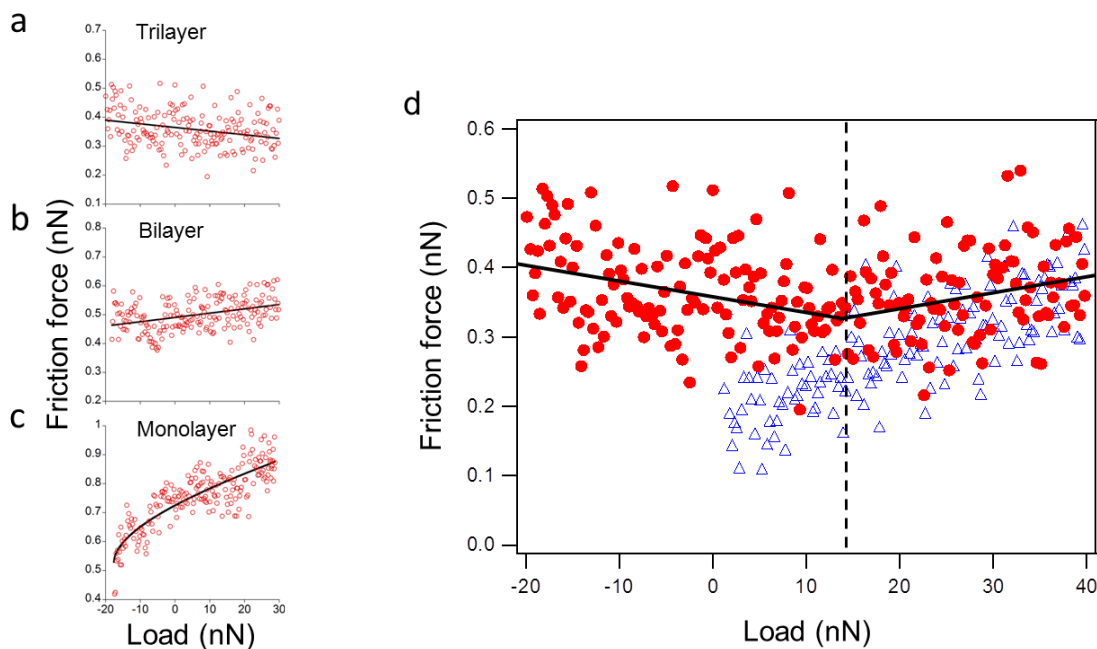


Figure S6 | Friction-load curves (retracting) taken on graphene supported by an SiO_2/Si substrate. Friction between **a**, trilayer, **b**, monolayer and **c**, bilayer graphene using the silicon nitride tip. Line fits serve as guides to the eye, indicating that the negative coefficient emerges as layers are added. **d**, The full approach (blue triangles) and retract (red filled circles) curves for the trilayer in (a). The onset of the negative coefficient occurs during retraction at loads below 15 nN, as determined from the point where the retract curve separates from the approach). The bilayer also exhibits a possible onset at -5 nN.

VI. XPS ANALYSIS OF THE AGED GRAPHITE SURFACE

The x-ray photoemission spectroscopy (XPS) measurements, performed in parallel with the friction-load experiments demonstrated that oxygen was chemisorbed to the graphite surface with exposure time in laboratory air, as discussed in the main text. Figure S7a shows the evolution of the oxygen content (O1s atomic %), where the remaining content is attributed to the carbon 1s peak (not shown). No nitrogen or other species could be identified by XPS.

Figure S7b shows the emergence of two oxygen 1s region peaks as surface oxygen content grew. The peak at (531.9 ± 0.2) eV was observed to emerge shortly following the peak at (533.1 ± 0.2) eV. These peaks have been shown to correspond to O_2 chemisorption and H_2O wetting^{S22}, respectively, and they emerge simultaneously as a result of O_2 adsorption forming a more hydrophilic surface than freshly cleaved graphite^{S23}. We believe this increases tip-sample adhesion through greater electrostatic interaction and possible meniscus formation.

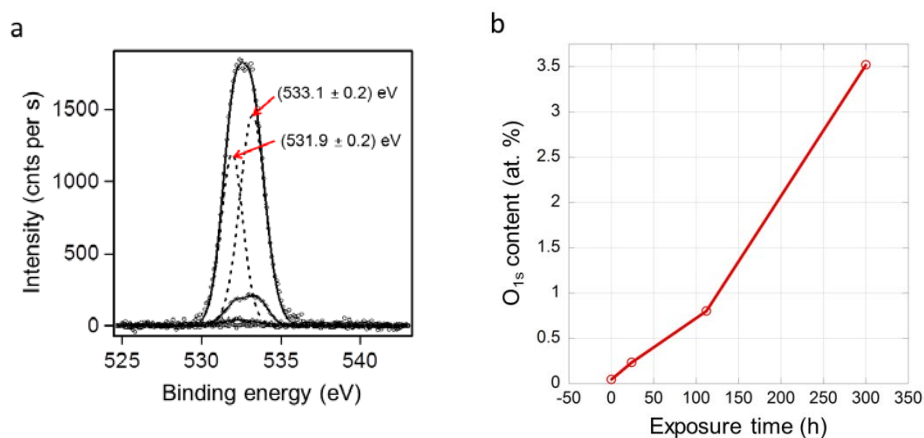


Figure S7 | **a**, XPS spectra (open circles) showing O_2 chemisorption (≈ 532 eV) and H_2O wetting (≈ 533 eV) peaks (both dashed lines) emerging as a function of exposure time in laboratory air. **b**, Corresponding surface oxygen content (total O_{1s} peak intensity from solid line-fit in (a)) as a function of exposure time.

VII. LINEAR DEPENDENCE OF FRICTION ON LOAD

We note that the friction force at a given load increased linearly with the magnitude of the adhesive force, $|L_C|$. Figure S8 shows two load examples ($L = 0$ nN and 40 nN) for the 30 nm radius diamond probe on graphite, where different exposure times have been combined to produce the variation in L_C , as in Fig. 2 of the main text. α exhibited a stronger than linear

dependence on $|L_C|$ (Fig. 2a), while the friction force at a given load varied linearly with L_C (Fig. S8). Assuming friction is proportional to contact area, the nonlinear behavior of α cannot be accounted for by a straightforward scaling with contact area, as that would require α to have a linear dependence on L_C , as well. For example, normalization of α vs. L_C to the corresponding friction at zero load, F_0 , (thus, to the presumed contact area) does not collapse the friction-load plots (*e.g.*, Fig. 1) onto a single line. As shown in Fig. S8b, an L_C -dependent slope remains, as a result of a more fundamental change in the tip-sample interaction and the mechanical behavior of the top surface layer.

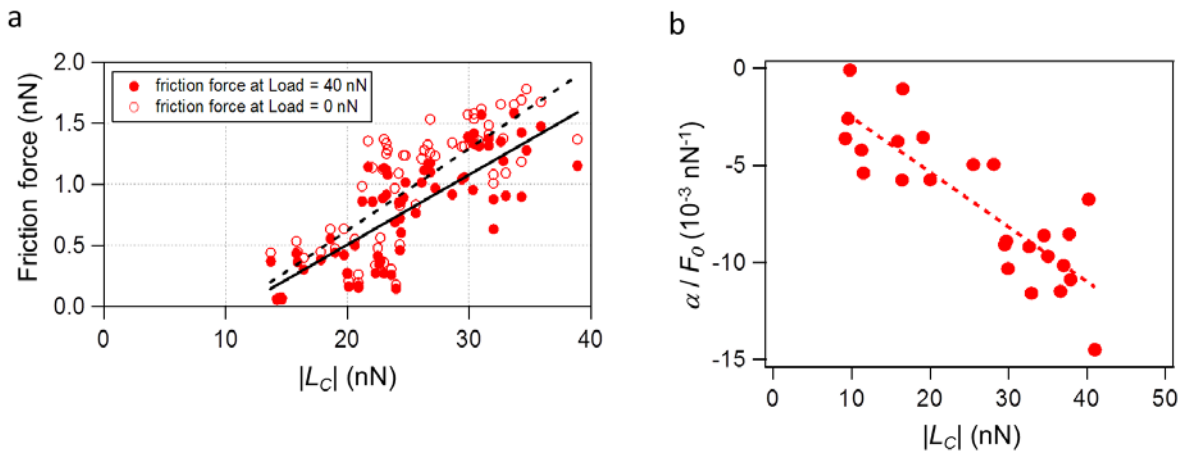


Figure S8 | Linear dependence of friction force on adhesive force. a, Friction is plotted versus the magnitude of the adhesive force, $|L_C|$, for zero applied load and a load of 40 nN. **b,** Normalization of α to F_0 yields linear behavior, suggesting α is not directly related to contact area.

Based on the linearity of the friction-load data during tip retraction and the corresponding increase in FEM-simulated barrier height, it may be possible to represent the deformation of the top layer while sliding by an existing plowing model previously established for surfaces coated

by Langmuir-Blodgett layers^{S24}. As is typical of continuum models, this approach begins by assuming a proportional relationship between friction, F , and contact area, A :

$$F = \tau A, \quad (\text{S1})$$

where τ is the interfacial shear strength. When rippling or plowing occurs, τ is pressure-dependent, *i.e.*, $\tau = \tau_{int} + \alpha P$, with P the average contact pressure, α a constant (herein referred to as the nanoscale friction coefficient), and τ_{int} the intrinsic interfacial shear strength. With $P = L/A$, equation (S1) may be written as

$$F = F_{int} + \alpha L, \quad (\text{S2})$$

where the interfacial term $F_{int} \equiv \tau_{int} A$, $F_0 \equiv F_{int}(L=0)$, and A depends on L_C . For continuum models of single asperity contacts, $A(L=0) \propto L_C^{4/3}$; however, the observed linear dependence of F_0 on L_C (section VII) suggests that the contact area follows a different relation. The second term in equation (S2) represents the rippling of the lifted graphene layer. This pressure-dependent term assumes an increase in material pile-up, *i.e.*, more material impeding lateral motion, with load. Though originally understood to be a positive value, indicating greater rippling at *higher* loads, we observed larger deformations on graphite as the applied load was *reduced*. The strong linear dependence of friction on applied load during retraction suggests that the plowing term dominates at the onset of lifting, where this term represents the compressive stresses at the outermost edges of the tip-sample contact.

VIII. SIMULATIONS SUPPLEMENT

A. MD

Movie S1 shows a cross-sectional view of the CNT tip sliding on the graphite substrate for the 5:1 enhancement under an applied load of -6 nN. A deformed (lifted) region follows the tip position as it slides over the surface.

Figure S9 shows the vertical deflection data from Fig. 4a (5:1 at -6 nN applied load) along with the corresponding deflection profiles for a load of 0 nN.

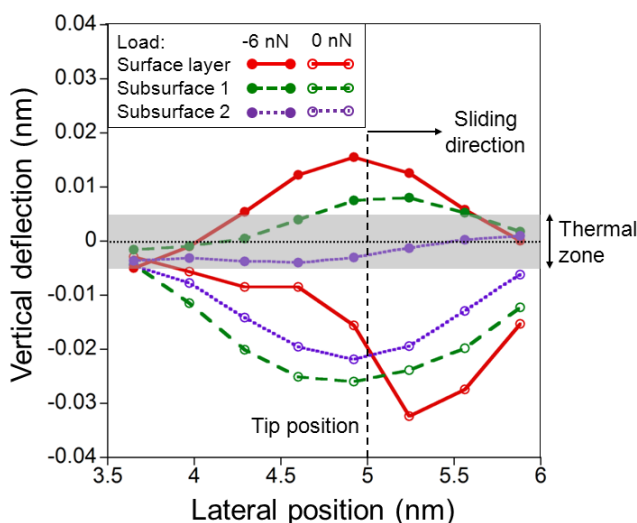


Figure S9 | MD vertical deflection profiles (out-of plane deviation from average height) of the three topmost graphene layers during sliding. Deflections are shown for zero applied load and just prior to pull-off (-6 nN load) for the 5:1 tip-graphene to graphene-graphene interaction ratio. The profiles have been shifted so that 0 on the vertical axis corresponds to their zero deflection positions. The gray zone refers to the region over which thermally excited deflections occur naturally at room temperature.

B. FEM

Movies S2-S5 show FEM-simulated profiles during sliding at displacements of 0.27 nm, 0.33 nm, 0.37 nm, and 0.43 nm (from pressing to lifting) for the 3:1 case, where tensile and compressive stresses are indicated by a corresponding color gradient. Comparing lifting (*e.g.*, Mov. S5) with pressing (*e.g.*, Mov. S2) while sliding, the lifting case leads to the transfer of the most compressive stresses from the central region around the tip apex to the outer perimeter of the contact zone. We note that this new stress distribution could lead to a different functional form for the area-load relation than a regular centrally compressed contact configuration. When the tip retracts, the central contact area reduces quickly at the beginning and later gradually levels off because of the lateral spread in the lifted region (Fig. 4c). However, because of the enlarged lifted region, more force is needed to push the enlarged lifted region forward. This mechanism, together with the increase in out-of-plane deformability of the lifted layer, leads to the usual increase in friction. We note that this result is derived from the continuum assumption of an interfacial shear stress in our FEM model. Although a complete understanding of the process may require combination of both continuum and atomistic analyses, our FEM results demonstrate that a reversible partial delamination of the topmost atomic layer(s) can indeed lead to this unusual friction behavior.

As mentioned above, in a load-controlled experiment, pull-off would occur at the minimum load. In this displacement-controlled simulation, we calculated friction at several additional displacement values for each data set to capture the contact behavior under retraction at displacements beyond the maximum tensile load (pull-off) points shown in Fig. 4d. Fig. S10 combines the friction data of Fig. 4d with these additional data—all plotted as a function of tip-sample displacement (Fig. S10a) and calculated normal load (Fig. S10b). A dip and abrupt rise

in friction upon retraction in the 2:1 case is followed by a slope lower in magnitude than in the 3:1 case. This intermediate behavior is a result of a competition between adhesion of the graphene layer to the substrate versus the tip, leading to changes in the amount by which the rippling increases with retraction. In the typical behavior for a JKR-like contact between isotropic materials, friction decreases with decreasing contact area, even as the normal load increases again after what would be the pull-off point in a load-controlled experiment^{S21,S25}. Conversely, Fig S10 shows that friction increases in this regime. We believe friction would eventually decrease again, as the tip fully separates from the substrate.

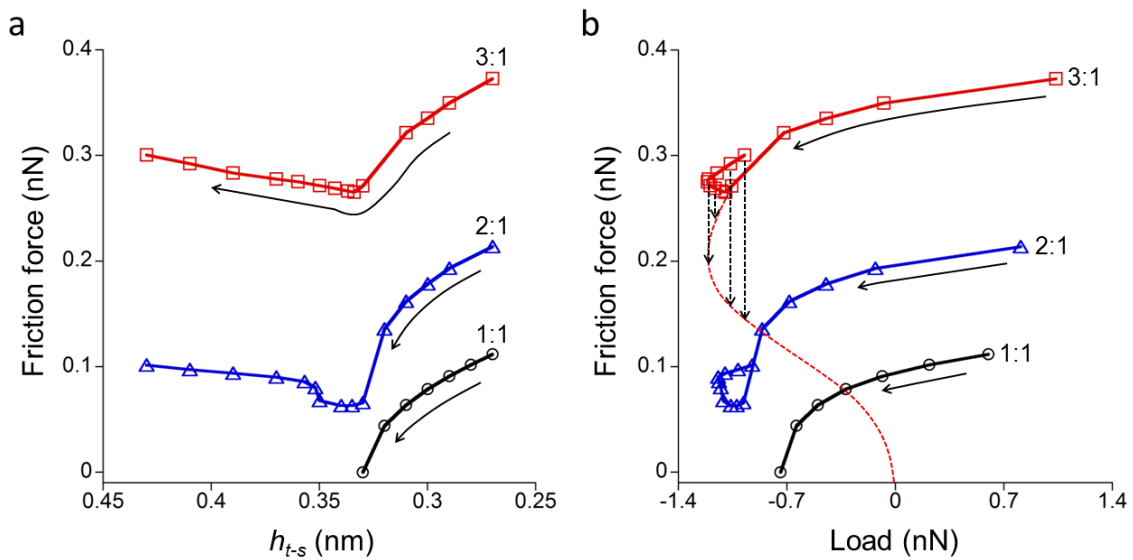


Figure S10 | FEM simulation results for friction beyond the maximum tensile load. a,

Friction force as a function of tip-substrate displacement, h_{t-s} , during retraction (solid arrows) for different enhancement ratios up to the same maximum tip-substrate displacement

($h_{t-s} = 0.43$ nm); the graphene layer and substrate are located at $h_{t-s} = 0.33$ nm and $h_{t-s} = 0$,

respectively. **b,** The same data plotted as a function of average normal load. The curve turns

around at the maximum tensile load (pull-off point in AFM), after which the load increases with

increasing h_{t-s} while the total contact area continues to decrease. A JKR-like plot (red dashed line) qualitatively illustrates what might be expected for a typical (isotropic) system with similar pull-off force and positive load behavior. For comparison, dashed arrows indicate how four of the data points might map onto the JKR curve.

References for Supplementary Information

- S1. Li, Q., Kim, K.-S. & Rydberg, A. Lateral force calibration of an atomic force microscope with a diamagnetic levitation spring system. *Rev. Sci. Instrum.* **77**, 065105 (2006).
- S2. Hutter, J. L. & Bechhoefer, J. Calibration of atomic-force microscope tips. *Rev. Sci. Instrum.* **64**, 1868-1873 (1993).
- S3. Lantz, M. A., O'Shea, S. J., Hoole, A. C. F. & Welland, M. E. Lateral stiffness of the tip and tip-sample contact in frictional force microscopy. *Appl. Phys. Lett.* **70**, 970-972 (1996).
- S4. Carpick, R. W., Ogletree, D. F. & Salmeron, M. Lateral stiffness: A new nanomechanical measurement for the determination of shear strengths with friction force microscopy. *Appl. Phys. Lett.* **70**, 1548-1550 (1997).
- S5. Smolyanitsky, A., Killgore, J. P. & Tewary, V. K. Effect of elastic deformation on frictional properties of few-layer graphene. *Phys. Rev. B* **85**, 035412 (2012).
- S6. Brenner, D. W. Empirical potential for hydrocarbons for use in simulating the chemical vapor deposition of diamond films. *Phys. Rev. B* **42**, 9458-9471 (1990).
- S7. Zacharia, R., Ulbricht, H. & Hertel, T. Interlayer cohesive energy of graphite from thermal desorption of polyaromatic hydrocarbons. *Phys. Rev. B* **69**, 155406 (2004).

- S8. Hasegawa, M., Nishidate, K. & Iyetomi, H. Energetics of interlayer binding in graphite: the semiempirical approach revisited. *Phys. Rev. B* **76**, 115424 (2007).
- S9. Spanu, L., Sorella, S. & Galli, G. Nature and strength of interlayer binding in graphite. *Phys. Rev. Lett.* **103**, 196401 (2009).
- S10. Jiang, L. Y., Huang, Y., Jiang, H., Ravichandran, G., Gao, H., Hwang, K. C. & Liu, B. A cohesive law for carbon nanotube/polymer interfaces based on the van der Waals force. *J. Mech. & Phys. Sol.* **54**, 2436-2452 (2006).
- S11. Lee, C., X. D. Wei, J. W. Kysar & Hone, J. Measurement of the elastic properties and intrinsic strength of monolayer graphene. *Science* **321**, 385-388 (2008).
- S12. Yakobson, B. I., Brabec, C. J. & Bernholc, J. Nanomechanics of carbon tubes: Instabilities beyond linear response. *Phys. Rev. Lett.* **76**, 2511-2514 (1996).
- S13. Scarpa, F., Adhikari, S., Gil, A. J. & Remillat, C. The bending of single-layer graphene sheets: the lattice versus continuum approach. *Nanotechnology* **21**, 125702 (2010).
- S14. The full description of the procedures used in this paper requires the identification of certain commercial products and their suppliers. The inclusion of such information should in no way be construed as indicating that such products or suppliers are endorsed by NIST or are recommended by NIST or that they are necessarily the best materials, instruments, software or suppliers for the purposes described.
- S15. Dienwiebel, M., Verhoeven, G. S., Pradeep, N. & Frenken, J. W. M. Superlubricity of graphite. *Phys. Rev. Lett.* **92**, 126101 (2004).
- S16. Dienwiebel, M., Pradeep, N., Verhoeven, G. S., Zandbergen, H. W. & Frenken, J. W. M. Model experiments of superlubricity of graphite. *Surf. Sci.* **576**, 197-211 (2005).

- S17. Socoliuc, A., Bennewitz, R., Gnecco, E. & Meyer, E. Transition from stick-slip to continuous sliding in atomic friction: entering a new regime of ultralow friction. *Phys. Rev. Lett.* **92**, 134301 (2004).
- S18. Medyanik, S. N., Liu, W. K., Sung, I.-H. & Carpick, R. W. Predictions and observations of multiple slip modes in atomic-scale friction. *Phys. Rev. Lett.* **97**, 136106 (2006).
- S19. Johnson, K. L. & Woodhouse, J. Stick-slip motion in the atomic force microscope. *Tribol. Lett.* **5**, 155-160 (1998).
- S20. Koenig, S. P., Boddeti, N. G., Dunn, M. L. & Bunch, J. S. Ultrastrong adhesion of graphene membranes. *Nature Nanotechnol.* **6**, 543-546 (2011).
- S21. Johnson, K. L., Kendall, K. & Roberts, A. D. Surface energy and the contact of elastic solids. *Proc. R. Soc. Lond. A* **324**, 301-313 (1971).
- S22. Marchon, B., Carrazza, J., Heinemann, H. & Somorjai, G. A. TPD and XPS studies of O₂, CO₂, and H₂O adsorption on clean polycrystalline graphite. *Carbon* **26**, 507-514 (1988).
- S23. Wang, S., Zhang, Y., Abidi, N. & Cabrales, L. Wettability and surface free energy of graphene films. *Langmuir* **25**, 11078 (2009).
- S24. Briscoe, B. J. & Evans, D. C. B. The shear properties of Langmuir-Blodgett layers. *Proc. R. Soc. Lond. A* **380**, 389-407 (1982).
- S25. Burns, A. R., Houston, J. E., Carpick, R. W. & Michalske, T. A. Friction and molecular deformation in the tensile regime. *Phys. Rev. Lett.* **82**, 1181-1184 (1999).